Roughness spatial reconstruction algorithm of DT layer in cryogenic targets using optical technics

A. CHOUX*[1], L. JEANNOT**[1], F.GILLOT[1], F. SANDRAS[1], M. MARTIN[1], C. GAUVIN[1], G. PASCAL[1], E. BUSVELLE[2], J.P. GAUTHIER[2], P.BACLET[1]

[1]CEA, centre de Valduc, Département de recherche sur les matériaux nucléaires, Service Microcibles, 21120 Is Sur Tille, France.

[2] Université de Bourgogne, LE2I UMR CNRS 5158, 21000 Dijon, France.

*e-mail : alexandre.choux@cea.fr (corresponding author)

**e-mail : laurent.jeannot@cea.fr (corresponding author)

ABSTRACT

The measurements of the solid DT layer, in terms of thickness and roughness, in the LMJ geometry (i.e. in a hohlraum) are not trivial. The DT layer measurements will be done using a Matsukov-Cassegrain telescope placed 39 cm away from the target. This telescope will be used to acquire shadowgraphy images on equators, and interferometric measurements on pole areas using optical coherence tomography (OCT).

Optical coherence tomography allows determining the DT layer thickness on a few points, in the polar regions of the target. By scanning around the poles, several points can be acquired in order to calculate the roughness and the local shape of the DT layer at the pole. Both technics were demonstrated on a 175 µm thick microshell with a 100 µm thick D_2 layer.

A reconstruction algorithm was designed to give the whole shape of the DT layer from the partial data given by shadowgraphy and OCT. A 3 D spatial estimation of the DT layer can be obtained. The algorithm efficiency was improved, with the use of 360 points on shadowgraphic image and 11 points on each pole. An estimation of the spatial DT layer shape was given on the first 90 longitudinal modes and on the first 5 equatorial modes.

I. INTRODUCTION

The Laser-Megajoule project (LMJ) is the french project on inertial confinment [1]. The thermonuclear fusion shall be obtained by the implosion of a solid deuterium-tritium (DT) fuel layer inside a plastic spherical shell. This cryogenic target is a 100 μm thick layer of solid deuterium-tritium at 18.2 K uniformly distributed around the inner surface of a 175 μm thick spherical polymer shell with 2430 μm in diameter. This one is located at the center of a cylindrical hollow cavity.

The ice layer is conformed by natural self heating due to the radioactive decay of tritium, called β-layering. The DT sublimates from the thicker parts of the layer and recrystallizes and deposites on the thinner parts of the layer. The β-layering is more detailed in [2, 3]. The conformation of the DT-layer can be optimized by precise control of the thermal environment of the shell.

In order to achieve ignition by inertial confinement fusion, the physicist's requirements for DT-layer thickness and roughness are extremely stringent. If the DT layer is perturbed by any thermal effect, or if the roughness is too important, some hydrodynamics instabilities could happen during the implosion. For these reasons, the DT-ice quality has to be known precisely.

The DT-layer can be observed only through a pair of laser entry holes in the lateral face of the cylindrical cavity. This is the major constraint that restricts the possibility to get information on the thickness of the solid DT layer. Therefore optical shadowgraphy is relevant to measure the DT inner surface along an equator located in a plane perpendicular to the optical axis. Other measurements are obtained by interferometry [4] and provide direct measurements of the thickness of the DT-layer in a small region near the optical axis (called the poles here in).

The content of the paper is as follows:

First of all, the principle of the optical shadowgraphy will be reminded in the case of our system. We will notice the appearance of a series of bright rings (caustics) corresponding to several types of optical paths. In the paper, we will focus on the main bright ring only. We will show how to establish the equation of this ring in the ideal case of a perfectly spherical and centered DT-layer.

Figure 1

The ideal bright ring is subject to certain perturbations that we assume to be small. The detection of the perturbed bright ring and its analysis will be detailed.

There is a link between these perturbations and the perturbations of the inner surface of the DT-layer. The main fact is that, as caustics, the rings give information not only on the shape of the inner surface, but also on its tangent planes. Linearized formulas of this link will be stated. More details on all formulas are given in [5].

On a second part, an interferometric method will be described to make thickness measurements near the target poles.

At the end, we will conciliate two types of information: 1) the information along the equator, of the perturbations of the DT-layer and the perturbations of its tangent planes, and 2) the direct interferometric measurements at the pole. We will therefore obtain, thanks to an interpolation approximation procedure, a final expansion of the inner surface of the DT-layer in terms of spherical harmonics.

II. SHADOWGRAPHY

II.1. Ideal caustic

The optical shadowgraphy is a technique which consists in putting the studied object between a light source and a camera. The collimated light comes from a source and goes through the cavity to the camera. The pictures that are obtained show the shadow of the illuminated object, as we can see on the figure 2. Due to both the spherical shell and the DT-layer, light rays from the source use several optical paths, of different energy. Then they intersect the camera sensor and we can catch some images.

Figure 2

Figure 3

Figure 3 shows the optical path that will be considered in the shadowgraphic system: light rays go from the left to the right. The rays on the right of figure 3, after crossing the entire optical device give a lighted caustic [9, 10]. The intersection of this caustic with the camera sensor draws a bright ring as seen on figure 2 when the image of the microshell equator is on the sensor.

As explained before, we exploit only the main ring, i.e. the one with maximum light energy. The corresponding theoretical caustic is a perfect circle due to the cylindrical symmetry of the system around the optical axis.

Let us now give the form of the parametric equation of the theoretical caustic. Because of the cylindrical symmetry, calculations can be done in any plane containing the optical axis. If u is the

longitudinal distance from the camera sensor, let $\rho \to R_u^*(\rho)$ be the map in which a ray from the left (at axial distance ρ from the optical axis) associates the axial distance from the optical axis of the intersection of the corresponding ray on the right with the plane of the sensor.

This map has the following form:

$$R_u^*(\rho) = h_1(\rho) + u h_2(\rho), \tag{1}$$

where $h_1(\rho)$ and $h_2(\rho)$ are smooth functions with respect to the variable ρ, depending on the optical parameters of the global considered system (refractive indexes, curvature radius of diopters, …).

Then the intersection of the caustic in the u-plane is given by:

$$\frac{\partial R_u^*}{\partial \rho} = 0 \tag{2}$$

When the camera sensor is located on the microshell equator image ($u = 0$), we note ρ^* the axial distance from the optical axis of the microshell incident ray that intersects the sensor plan on the theoretical ideal caustic (by cylindrical symmetry around the optical axis all these rays give a bright ring).

Then, the radius of the (ideal) bright ring in the u-plane is

$$R_c = h_1(\rho^*) \tag{3}$$

Since we consider only one type of optical path (the most energetic one), the energy of each ray is supposed to be the same. Hence we can compute, (by numerical simulation), an irradiance map, giving the ideal lighting of the plane-optical-sensor. Along a radial profile on the sensor plane, we can get an intensity profile.

The calculated position of the intersection of the caustic with the sensor plane corresponds to a wall of intensity. This fact will be exploited for practical detection of the caustic.

II.2. Bright ring analysis

With the results of the next paragraph, using the caustic (see figure 2), we will reconstruct precise information about the inner surface of the DT-layer and its tangent plane on a circle close to the equator plane.

$r(\theta)$ is the polar equation of the intersection of the inner surface of the DT layer with the microshell equator plane. The DT 2D roughness is defined as the fraction of the power spectral density of the Fourier decomposition of $r(\theta)$ corresponding to high harmonics.

We assume as a first approximation that $r(\theta)$ is proportional to the polar equation of the main caustic. Therefore, having reconstructed the main caustic, we can perform standard Fourier analysis to compute some approximation of the 2D roughness.

Standard zero-crossing technique can be used to detect precisely the caustic. We used the very classical method of [8], which keeps all the images data safe after filter treatment.

Starting from the outer board of the microshell, we encounter few zeros in the laplacian image treatment (see figure 4): the first one corresponds to the shell outer diopter, the second one to the

outer smooth board of the ligth rays concentration close to the caustic, the third one is the vertical jump of the caustic and the other zeros correspond to other secondary caustics from different optical paths. So the aim of our method is to find the third zeros positions.

This one is determined by taking a pixel with positive value and another with negative value around the zero on the profile. Thereby the zero is defined as the weighted barycentre of these two pixels. Using an algorithm following the zeros in the neighborhood of a starting point, the whole caustic-shape is extracted.

Thereafter the points are approximated (interpolated with C^2-splines) on the circle using the least square method (it happens that typically there are large holes on real bright rings, presumably due to non-C^1 perturbations of the inner DT solid surface).

The resulting approximation will be used in the next sections for the global reconstruction of the inner shape of the DT-layer. Moreover, Fourier analysis of this approximation is supposed to provide the 2D DT solid roughness.

Figure 4

II.3. Shadowgraphic analysis

Figure 5

The solid DT layer will always get perturbations on the inner surface (figure 5) , thus the main bright ring will be disturbed. Disturbances on one point of the inner surface can be modelled by a perturbation ε_1 on the radius of the inner sphere, a perturbation ε_2 on the normal vector in the plane (P) determined by the point and the optical axis, and another ε_3 in the plane perpendicular to (P). In fact, ε_2 is the component (in a natural moving orthonormal frame) of the perturbation, in the direction which is parallel to the tangent of our surface in the (P) plane. At first order, it is the same as a (natural) angle between the ideal normal and its perturbation. These perturbations are assumed to be smooth and small in the C^1 sense.

In the following, the notation O^i refers to expressions of order i in $\varepsilon_1, \varepsilon_2, \varepsilon_3$ and their first derivatives.

Note that these three perturbations are not independent. This fact has no consequence on the theoretical results in this section. But, it will be implicitly taken into account when we will merge the whole data by a least square method.

$\mathbb{R}$ Let $\rho \in$ and $\theta \in [0,2\pi[$ be the polar coordinates of the starting collimated light ray in a plane perpendicular to the optical axis.

$\mathbb{R}$ Let $R \in$ and $\alpha \in [0,2\pi[$ be the polar coordinates of the light ray crossing the optical sensor (in its own plane).

Let $R^*(\rho)$ denote the distance to the origin of the intersection point of a ray (starting with

coordinate ρ) with the sensor-plane, in the ideal unperturbed situation.

The following equations are a consequence of both the axial symmetry of the ideal situation and the required smoothness of the perturbation. The proof is just writing explicitly the expansion of the successive optical refractions and reflections. It is a straightforward but tedious computation. It has been checked by using Mathematica.

$$R(\rho,\theta) = R^*(\rho) + a_1(\rho)\varepsilon_1(\rho,\theta) + a_2(\rho)\varepsilon_2(\rho,\theta) + O^2 \tag{4}$$

$$\alpha(\rho,\theta) = \theta + a_3(\rho)\varepsilon_3(\rho,\theta) + O^2 \tag{5}$$

for certain smooth real functions a_1, a_2, a_3.

Note that the functions a_1, a_2, a_3 depend only on the properties of the optical system.

For the same reasons (symmetry of the ideal situation, and smoothness of the perturbations), the following equation is easily proved:

The equation of the caustic is

$$\frac{\partial R}{\partial \rho} = 0 \tag{6}$$

Now, we will compute the first order expansion of the caustic of the perturbed system. Let ρ^*

denote the radial coordinate of the starting rays of the unperturbed system, intersecting the sensor plane on the ideal caustic. Let φ^* denote the corresponding angle between the ideal ray [from the center of the microshell to the DT-layer] and the optical axis.

The equation at order 1 of the perturbed caustic, in the coordinates (ρ,α) is given by:

$$R_c(\alpha) = R^*(\rho^*) + a_1(\rho^*)\varepsilon_1(\rho^*,\alpha) + a_2(\rho^*)\varepsilon_2(\rho^*,\alpha) + O^2 \qquad (7)$$

The second optical mean of characterization is an interferometric one that is described now.

III. OPTICAL COHERENCE TOMOGRAPHY

Optical coherence tomography (OCT) is used to measure the thickness of the DT layer on the polar regions of the capsules. This technique has been the object of many studies. OCT has been proved useful for biomedical imaging applications [12]. It is a new imaging technology that allows in vivo and in situ cross-sectional morphological imaging of transparent and nontransparent biological tissue on a micrometer scale [13]. OCT systems are typically implemented as Michelson interferometers with free-space or fiber optics, where one of the arms contains a sample to be measured, and the second contains a delay line that allows one to scan the relative time delay between the reference and the sample signals. Multiple, partially reflecting surfaces of the target can be detected during one scan of the delay line.

III.1. Measurement principle

OCT relies on the measurement technique of low coherence interferometry, which is also referred to as partial coherence tomography. The principle of operation is presented in a simplified way in figure 6. The light source is a super luminescent diode (SLD) with a (typical) centre wavelength λ_c=1310 nm and a bandwidth $d\lambda$ ranging from 30 nm to 60 nm FWHM (full width at half maximum), depending on the output power.

In the scheme of figure 6 the light is split by the coupler into the measurement arm and into the reference arm. Adjustable collimators are mounted at the exit of each fiber. To work on long distances, the collimator on the measurement arm is a QM100 Questar telescope .The reference arm contains the delay line where the light is reflected by a scanning mirror and coupled back into the fiber. The signals are reflected by the delay-line's mirror and by a reflecting interface in the target. They are combined on the detector where an interference signal is generated. It happens when the optical paths in the two interferometer arms match each other to within the coherence length of the light. Figure 6 shows in a simplified way, the interferometric signal (optical power versus delay line position) generated by the two reflecting interfaces in the target (reflections "R_1" and "R_2"). The absolute position of each interface can be determined from the delay line mirror position at the peak of the corresponding fringe packets.

The collimator (Questar telescope) focuses the measuring beam at a given distance. Choosing the "correct" focus position ensures that each surface in the optical system to be measured produces a significantly strong interference signal.

Figure 6

III.2. Theoretical description

For the theoretical description that follows we consider the situation depicted in figure 7. Starting from a rigorous mathematical description, one can derive the following approximation for the broad-band interferometric signal acquired by the OCT system.

Figure 7

$$I(Z) = \underbrace{exp[\,j2\pi\sigma_0 \cdot \{2n(\sigma_0)L - Z\}]}_{\text{sinusoidal\_fringes}} \cdot \underbrace{\exp\left[-4\ln(2)\frac{(Z - 2n_g(\sigma_0)L - Z)^2}{\tilde{l}_c^{\,2}}\right]}_{broadened\_Gaussian\_envelope} \cdot \underbrace{\exp[\,j\varphi_{chirp}(Z)]}_{chirp\_phase\_term}$$

The interferogram is expressed as a function of the optical path length Z in the reference arm

$$Z = 2n_{air}(\sigma_0)z$$

with the refractive index of air n_{air}. The sinusoidal fringe pattern has a spatial period (in Z) equal to $1/\sigma_0$ with σ_0 being the center wavenumber of the source spectrum that is assumed to be Gaussian with a FWHM $\delta\sigma$. Since $Z \sim 2z$, the fringe spacing expressed in delay line position z equals $1/2\sigma_0 = \lambda_0/2$.

The parameter $n_g(\sigma)$ is the wavenumber-dependent group refractive index, defined as

$$n_g(\sigma) = n(\sigma) + \frac{\partial n}{\partial \sigma} \cdot \sigma$$

The width (FWHM) of the envelope is given by

$$\tilde{l}_c = \sqrt{(2l_c)^2 + (2L \cdot GD_\sigma(\sigma_0) \cdot \delta\sigma)^2}$$

with the round-trip coherence l_c

$$l_c = \frac{2\ln 2}{\pi}\frac{{\lambda_c}^2}{\delta\lambda}$$

and with the group (velocity) dispersion GD_σ defined as

$$GD_\sigma(\sigma) = \frac{\partial n_g}{\partial \sigma} = 2\frac{\partial n}{\partial \sigma} + \sigma\frac{\partial^2 n}{\partial \sigma^2}$$

Group dispersion leads to a broadening of the coherence envelope, hence decreases the longitudinal resolution of the OCT. The latter is determined by the minimum distance between two reflecting interfaces such that their interferometric signal can still be separated.

III.3. First experimental validations on D_2

OCT system was tested on our direct drive cryostat with D_2 layer inside a CH microshell using collimation lenses at the end of each fiber. We obtained (see figure 8) the detection of the D_2 layer solid-gaz diopter inside a 175 µm thick microshell with a 206 µm thick D_2 layer. This detection was done around the pole of the capsule.

We obtained also (see figure 9) a double detection of the D_2 layer solid-gaz diopter in a 25 µm thick microshell. On the north pole (which met the light in first) the measured D_2 thickness was 109 µm and on the south pole it was 153 µm. This shows us a P1 mode [2] in this direction.
No thermal effect occurred during these tests and the accuracy of the measure was estimated by the OCT builder as 300 nm when the refractive index of the sample is perfectly known. This value need to be experimentally improved.

The integration of such a system in the Study Filling Station (for the study of cryogenic targets

in Valduc, CEA france) has begun and will use a Questar telescope in the measurement arm (see figure 10). These promising first results need to be confirmed on DT layers.

Figure 8

Figure 9

Figure 10

IV. DT LAYER ESTIMATION

Let us consider the previous angle θ and complete it with the other angle φ, in order to form Euler-like coordinates around the center of the microshell. Then, the inner surface of the DT-layer is modelled as a perturbation ε(θ, φ) of the ideal spherical inner surface of the DT-layer. As we said above, this perturbation is assumed to be C^2-small. It will be modelled a-priori as a finite sum of spherical harmonics

$$\varepsilon(\theta,\varphi) = \sum_{i=1}^{k} \lambda_i e_i(\theta,\varphi) \tag{8}$$

This is standard: disturbances of spheres are generally modelled by spherical harmonics [6], [7]. What is not standard here is our choice of the relevant spherical harmonics $e_i(\theta, \varphi)$. Here, we introduce some a-priori information. Practically, we consider only spherical harmonics that can occur in the physical configuration. Main perturbations have mainly three origins: 1) the gravity (the optical axis is in practice vertical), 2) the thermal disturbances coming from the two

windows of the cylindrical cavity, which are situated above and below the device, and 3) position errors of the center of the microshell w.r.t. the centre of the cylindrical cavity. Therefore, we will only keep spherical harmonics that give rise to these perturbations.

Note that this C^2-small disturbance $\varepsilon(\theta, \varphi)$ completely determines our perturbations $\varepsilon_1, \varepsilon_2, \varepsilon_3$ above.

At this point, our procedure for reconstructing the inner surface of the DT-layer $R+\varepsilon(\theta, \varphi)$ is performed in two different steps:

· First, we will reconstruct $\varepsilon_1(\rho^*, \theta)$, $\varepsilon_2(\rho^*, \theta)$, (and eventually $\varepsilon_3(\rho^*, \theta)$, but, as we said above, this looks unnecessary, the approximation $\theta=\alpha$ from relations (5, 7) being sufficient in practice).

Equivalently, we reconstruct $\varepsilon_1(\rho^*, \alpha)$, $\varepsilon_2(\rho^*, \alpha)$, $\varepsilon_3(\rho^*, \alpha)$, that is we reconstruct 1) the intersection of the perturbed inner surface of the DT-layer with the plane corresponding to ρ^*, perpendicular to the optical axis, 2) the tangent planes to the inner surface along this curve. This is 3D information (our main contribution).

· Second, we will reconcile this information with the information obtained at the poles, by direct optical coherence tomography measurements (our second main contribution).

Both steps are achieved by standard least square procedures.

- In the first step, the a-priori expansion (8) is used in restriction to (the plane)

$\{\varphi = \varphi^*\}: \varepsilon(\theta, \varphi^*) = \sum_{i=1}^{k} \lambda_i e_i(\theta, \varphi^*)$. As we said, we confuse this relation with the relation $: \varepsilon(\alpha, \varphi^*) = \sum_{i=1}^{k} \lambda_i e_i(\alpha, \varphi^*)$. Then, the practical measurements are the values $R_c(\alpha)$, that are considered equal to $R_c(\theta)$, and the main equation:

$$R_c(\alpha) \approx R^*(\rho^*) + a_1(\rho^*)\varepsilon_1(\rho^*, \alpha) + a_2(\rho^*)\varepsilon_2(\rho^*, \alpha), \quad (9)$$

from Equation (7) gives rise to a set of linear equations, with unknown's the λ_i's, i=1,...,k.

The number of equations is the number of values of α taken into account. The corresponding values $R_c(\alpha)$ come from the method, described in section II.2, to compute the inner part of the bright ring, corresponding to the caustic.

This overdimensionned system of linear equations is solved in the least-squares sense, and provides the curve [on the inner DT-layer, associated with the rays that intersect the caustic in the sensor plane] and the tangent plane to the inner surface along this curve.

-After that, we use this first information together with the direct measurements by OCT at the poles, and we reconcile both sets of data via a second standard least-squares step.

To finish, we show now some results of the full 3D Reconstruction of the inner surface of the DT-layer. Up to now, contrarily to the results of Section II.2 for the detection of the caustic, these are only simulation results, since we don't have yet the interferometric measurements at the poles.

The figure 11 shows a reconstructed inner surface of the DT-layer. For the same

reconstruction, figure 12 shows the real surface compared to the reconstructed surface, along a horizontal and a vertical cut. These deformations are not realistic but have been highlighted on the figures.

Figure 11

Figure 12

V. RECONSTRUCTION ALGORITHM OF THE SOLID DT LAYER

As we said before, the integration of the OCT system in the Study Filling Station has begun. Waiting for the first experiments on the DT layer, we collaborate with the Laboratory for Laser Energetic (LLE) from the University of Rochester [11]. D_2 and DT layers are observed in the "Omega" system. Each layer is characterized by about 50 views. All views are obtained by optical backlit shadowgraphy and cover the whole microshell, which can be rotated around its center.

In each shadowgraphic file, bright ring and microshell edge are described by 360 points (1 point per degree).

Choosing a view, we rotate all data to work like in the equatorial view of the microshell in the SFS. All points in the polar neighborhood are taking into account and are considered as interferometric data. We make 3 estimations of the perturbation on the D_2 layer considering with

the same set of points. In first, only half interferometric-data in both polar neighborhood are considered, in a second time the other half of the polar points are used and then all the interferometric data. For each estimation, all points of the chosen shadowgraphic-view are used. We found that the "equatorial" perturbations are identical for each evaluation, but not the "longitudinal" modes. Below are the results with a first file:

"longitudinal" mode	1st estimation	2nd estimation	3rd estimation
N°1	-1.68 µm	-2.15 µm	-1.84 µm
N°2	-1.90 µm	-1.42 µm	-2.28 µm
N°3	2.22 µm	2.73 µm	2.32 µm
N°4	-3.78 µm	-3.67 µm	-3.45 µm

So, we notice an error of 0.8 µm between the coefficients of these estimations. The error is probably due to the distribution of the points in the polar neighborhoods, that are located on straight lines as shown on the figure 13, in spite of randomly distributed with a normal-distribution law. We can add, that the polar point are considered as interferometric data and not as shadowgraphic data.

Figure 13

VI. CONCLUSION

To study the DT solid layer in a hollow cavity along some axial symmetry, backlit optical

shadowgraphy and optical coherence tomography seems to be relevant measurement methods. The shadowgraphic images show bright rings that are due to caustics. The detection of the main bright ring provides some 3 D information along a great diameter close to the equator perpendicular to the optical axis. Perturbation on the inner surface of the DT layer surface is link to the distortion of the bright ring by a linear relation.

OCT provides direct measurements on the polar neighborhood of the capsule. The first results show that its possible to measure D_2 thickness with OCT on the two poles of the microshell.

From the linear relation and the detection of the main bright ring, we get a partial 3 D estimation of the solid DT layer topography. Conciliating the shadowgraphic and interferometric data, an algorithm rebuilding the inner cryogenic layer is designed.

This algorithm has been validated using data send by the Laboratory for Laser Energetic.

We acknowledge W. Seka (Laboratory for Laser Energetics) for his collaboration.

Bibliography

1. J. D. Lindl, *Inertial Confinment Inertial*, (Springer, 1998)
2. J. Sater, B. Kozioziemski, J.J. Sanchez, G.W. Collins, E.R. Mapoles, J. Pipes, J. Burmann, "Cryogenic D-T fuel layers formed in 1 mm spheres by beta-layering", *Fusion Technology* **35** (March 1999).
3. M. Martin, C. Gauvin, A. Choux, P. Baclet, G. Pascal, "The cryogenic target for ignition on the LMJ: useful tools to achieve nominal temperature and roughness conditions of the DT layer", *Fusion Science and Technology* **49**, n°4, May 2006, 600-607.
4. F. Gillot, A. Choux, L. Jeannot, G. Pascal, P. Baclet, "Characterization of the DT layer of ICF targets by optical techniques", *Fusion Science and Technology* **49**, 626-634 (2006).
5. A. Choux, E. Busvelle, J.P. Gauthier, G. Pascal, “Observer for thick layer of Deuterium-Tritium using backlit optical shadowgraphy and interferometry”, submitted to Applied Optic.
6. E.W. Hobson, *The theory of spherical and ellipsoidal harmonics*, New York : Chelsea, 1955
7. H. Groemer, *Geometric applications of Fourier series and spherical harmonics*, Cambridge University Press, 1996
8. Marr, D. and Hildreth, E. "Theory of edge detection" *Proc. R. Soc. Lond. B*, 207, 1980, 187-217.
9. V. Zakalyukin, "Applications of flag contact singularities", *New Developments in Singularity theory*, Nato series, Kluwer, 2001, 41-70.
10. V.I. Arnold, A. Varchenko, and S. Goussein-Zadé. *Singularités des Applications*

Différentiables. I : Classification des Points Critiques, des Caustiques et des Fronts d'Onde. Editions Mir, Moscou, 1986.

11. D.H. Edgell, W. Seka, R.S. Craxton, L.M. Elasky, D.R. Harding, R.L. Keck, L.D. Lund, and M.D. Wittman, "Characterization of cryogenic direct-drive ICF targets during studies and just prior to shot time", to be published in *Fusion Science and Technology*.

12. D. Huang, E. A. Swanson, C. P. Lin, J. S. Schuman, W. G. Stinson, W. Chang, M. R. Hee, T. Flotte, K. Gregory, C. A. Puliafito, and J. G. Fugimoto, "Optical coherence tomography" Science 254, 1178-1181 (1991).

13. J. G. Fugimoto, C. Pitris, S. Boppart, and M Brezinski, "Optical coherence tomography, an emerging technology for biomedical imaging and optical biopsy" Neoplasia, 2, 9-25, January 2000.

Figures Captions

Figure 1. Environment of characterization of the ICF targets.

Figure 2. Shadowgraphic image of a target in an experimental environnement.

Figure 3. Optical path generating the main bright ring.

Figure 4. A radial profile on a laplacian treated image.

Figure 5. Used data on the shadowgraphic image.

Figure 6. Basic principle of the OCT system.

Figure 7. Schematic view of the measurement arm (top) and reference arm (bottom) of the OCT system.

Figure 8. Detection peak of a D_2 layer in a 175 µm thick capsule.

Figure 9. Detection peak of a D_2 layer in a 29 µm thick capsule.

Figure 10. 3D Scheme of the integration of OCT (interferometric fiber) in the study filling station using a Questar telescope.

Figure 11. A reconstructed deformation.

Figure 12. Comparison between cuts of original and reconstructed surfaces.

Figure 13. Distribution of the polar points.

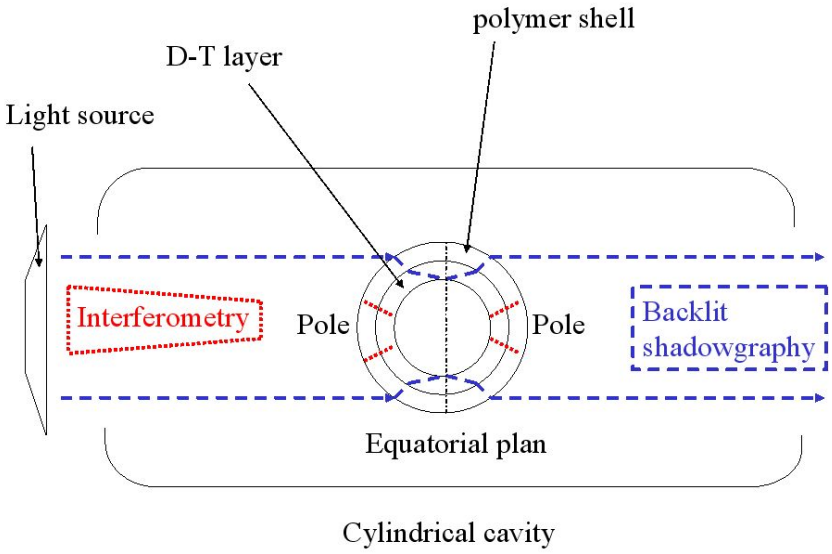

Figure 1. Environment of characterization of the ICF targets.

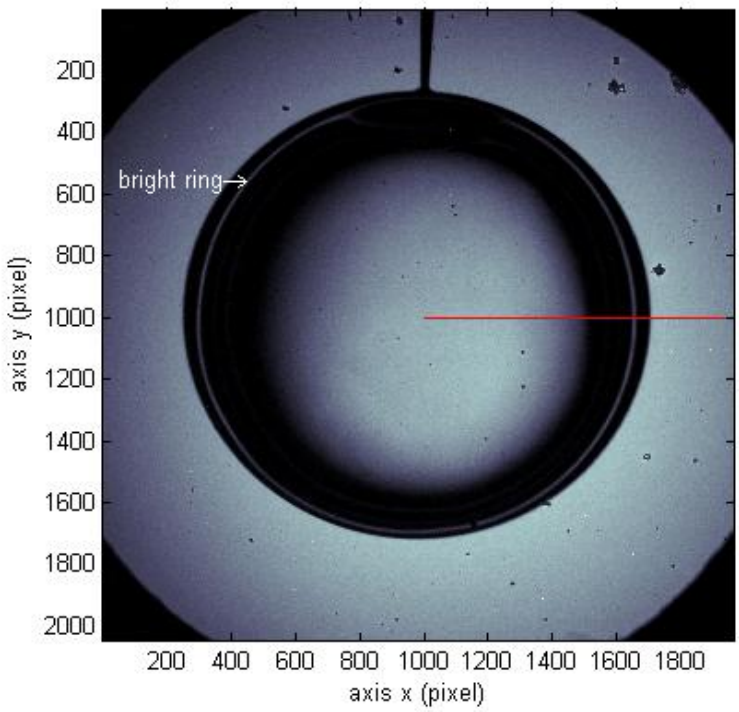

Figure 2. Shadowgraphic image of a target in an experimental environnement.

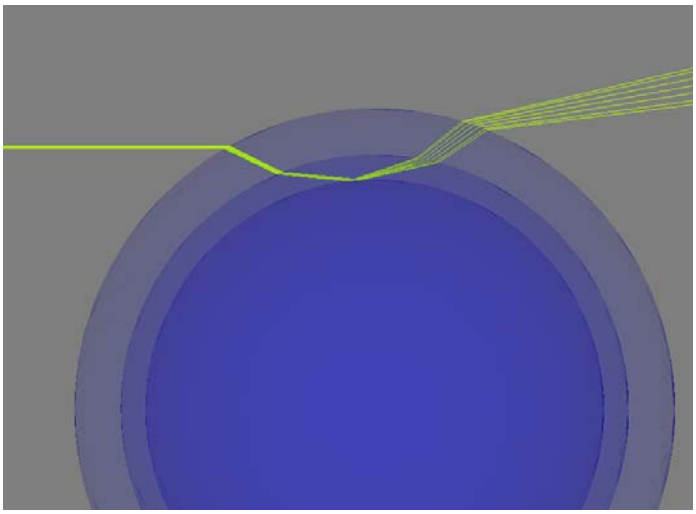

Figure 3. Optical path generating the main bright ring.

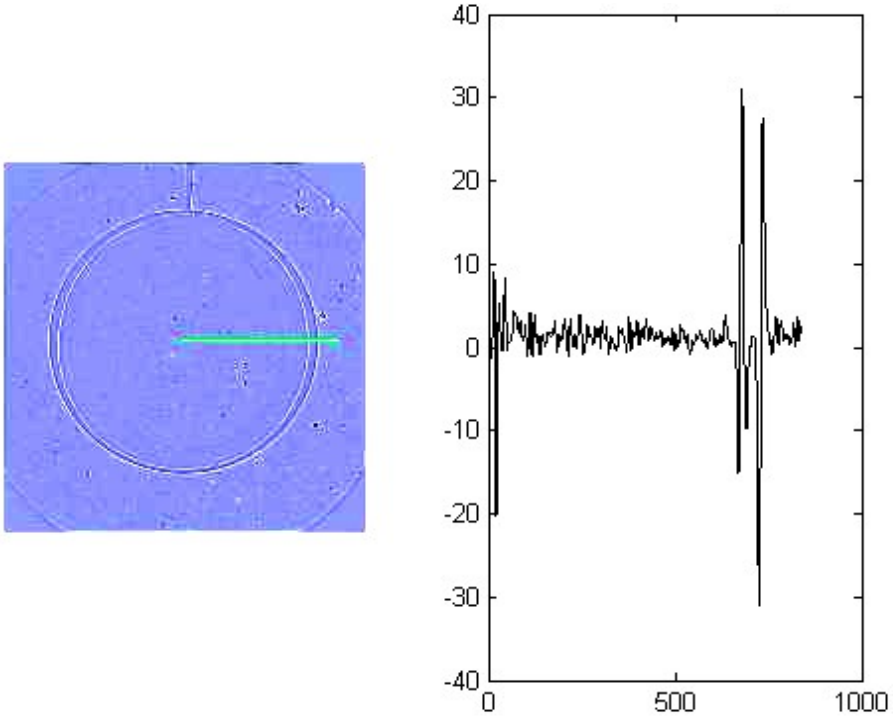

Figure 4. A radial profile on a laplacian treated image.

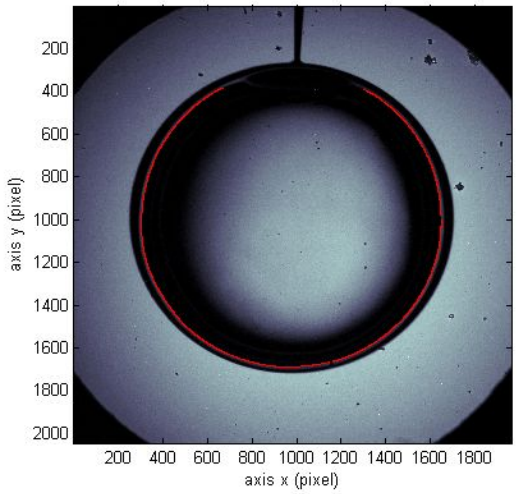

Figure 5. Used data on the shadowgraphic image.

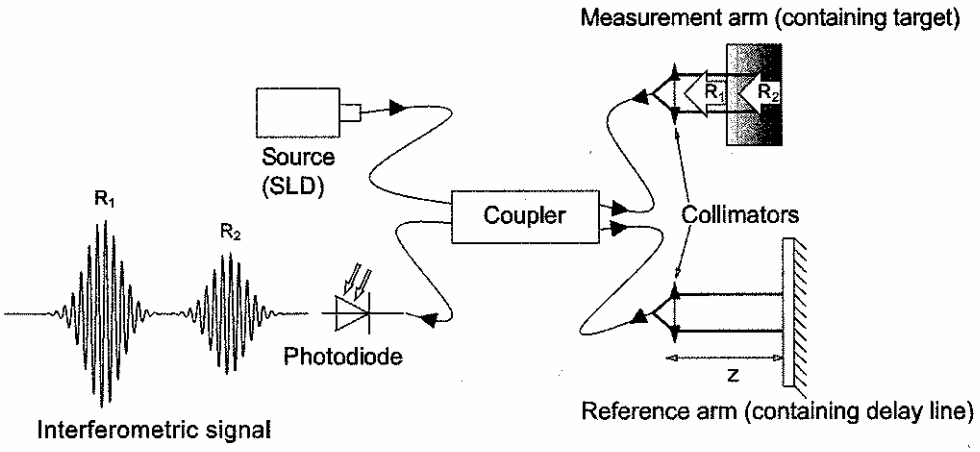

Figure 6. Basic principle of the OCT system.

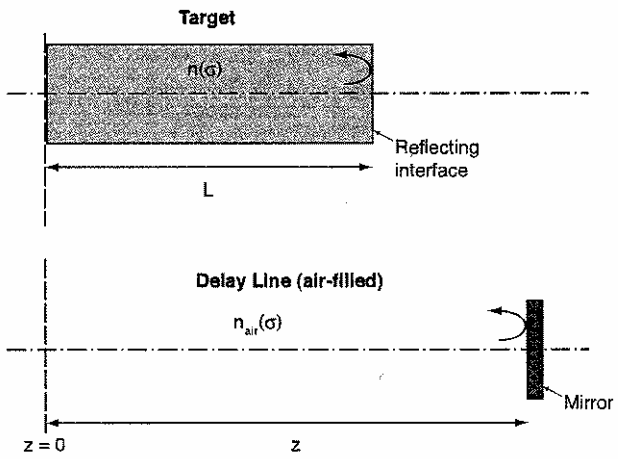

Figure 7. Schematic view of the measurement arm (top) and reference arm (bottom) of the OCT system.

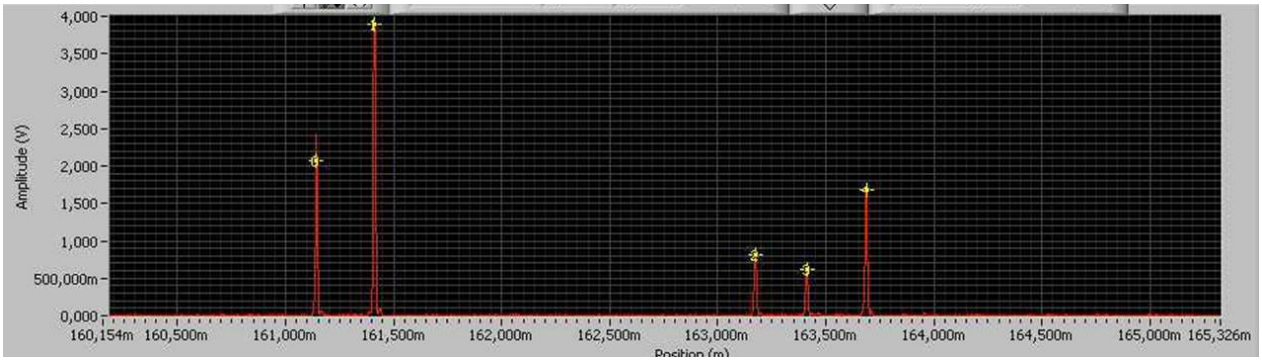

Figure 8. Detection peak of a D_2 layer in a 175 μm thick capsule.

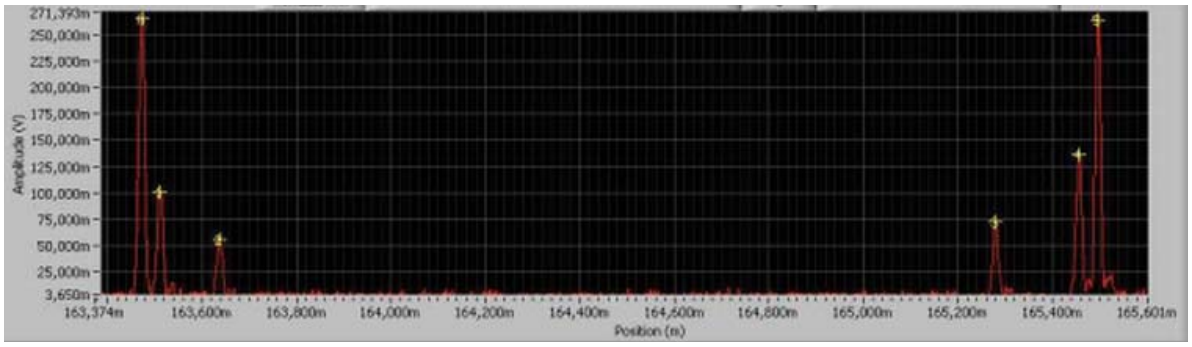

Figure 9. Detection peaks of a D_2 layer in a 29 μm thick capsule.

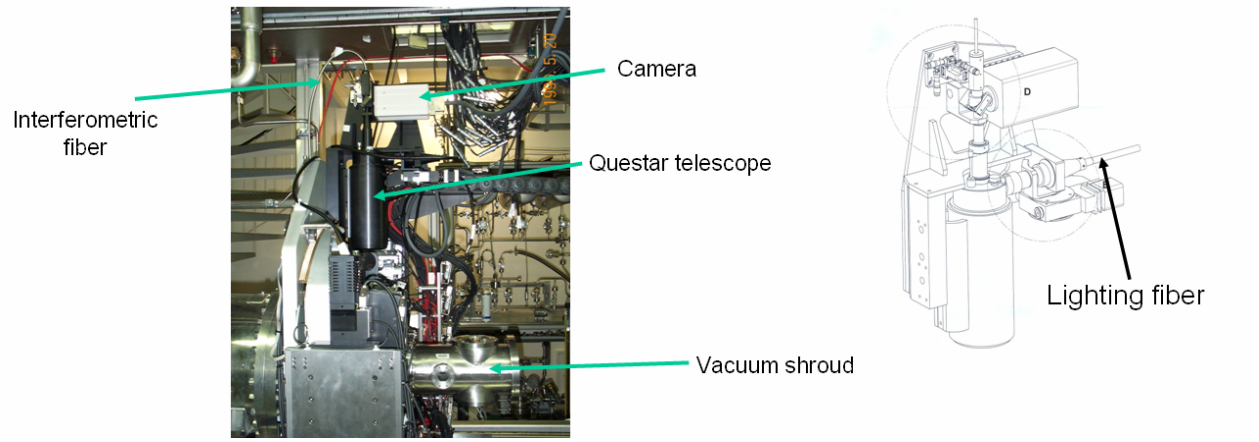

Figure 10. 3D Scheme of the integration of OCT (interferometric fiber) in the study filling station using a Questar telescope.

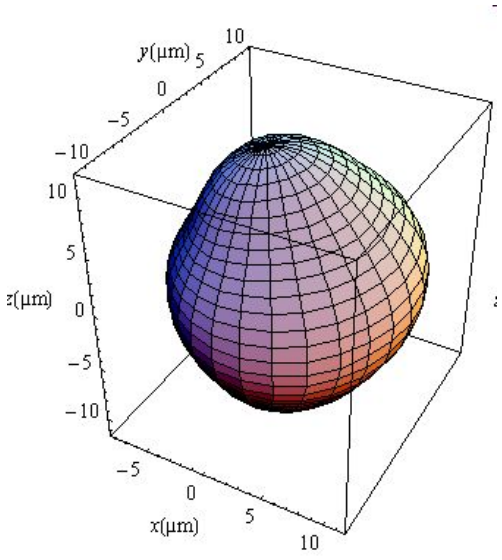

Figure 11. A reconstructed deformation.

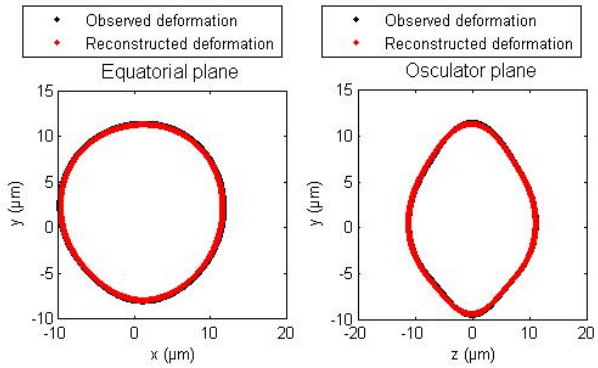

Figure 12. Comparison between cuts of original and reconstructed surfaces.

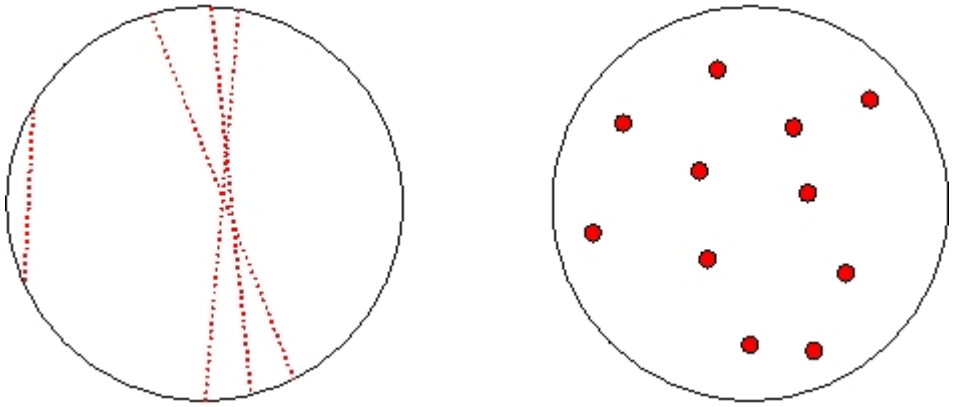

Figure 13. Distribution of the polar points:

- On the left-hand side: the distribution obtained with the LLE data,
- On the right-hand side: the wished distribution.